

# Strong-motion Broadband Displacements from Collocated Ocean-bottom Pressure Gauges and Seismometers

Ayumu Mizutani<sup>1</sup>, Diego Melgar<sup>2</sup>, and Kiyoshi Yomogida<sup>1</sup>

<sup>1</sup>Hokkaido University

<sup>2</sup>University of Oregon

December 27, 2023

## Abstract

Dense and broad-coverage ocean-bottom observation networks enable us to obtain near-fault displacement records associated with an offshore earthquake. However, simple integration of ocean-bottom strong-motion acceleration records leads to physically unrealistic displacement records. Here we propose a new method using a Kalman filter to estimate coseismic displacement waveforms using the collocated ocean-bottom seismometers and pressure gauges. First, we evaluate our method using synthetic records and then apply it to an offshore Mw 6.0 event that generated a small tsunami. In both the synthetic and real cases, our method successfully estimates reasonable displacement waveforms. Additionally, we show that the computed waveforms improve the results of the finite fault modeling process. In other words, the proposed method will be useful for estimating the details of the rupture mechanism of offshore earthquakes as a complement to onshore observations.

## Hosted file

981755\_0\_art\_file\_11673051\_s5czj0.docx available at <https://authorea.com/users/708312/articles/692941-strong-motion-broadband-displacements-from-collocated-ocean-bottom-pressure-gauges-and-seismometers>

1

2 **Strong-motion Broadband Displacements from Collocated Ocean-bottom Pressure**

3

**Gauges and Seismometers**

4

**Ayumu Mizutani<sup>1,2</sup>, Diego Melgar<sup>2</sup>, and Kiyoshi Yomogida<sup>1</sup>**

5

<sup>1</sup>Department of Earth and Planetary Sciences, Faculty of Sciences, Hokkaido University,

6

Sapporo, Japan.

7

<sup>2</sup>Department of Earth Sciences, University of Oregon, Eugene, Oregon, U.S.A.

8

Corresponding author: A. Mizutani ([mizutaniayumumail@gmail.com](mailto:mizutaniayumumail@gmail.com))

9

10 **Key Points:**

- 11
- Propose a new method to estimate the near-fault displacement waveform associated with
- 12 an offshore earthquake.
- 13
- The method utilizes the collocated strong-motion seismometer and ocean-bottom
- 14 pressure gauge.
- 15
- The obtained displacement waveforms improved the finite fault model.

16

17 **Abstract**

18 Dense and broad-coverage ocean-bottom observation networks enable us to obtain near-fault  
19 displacement records associated with an offshore earthquake. However, simple integration of  
20 ocean-bottom strong-motion acceleration records leads to physically unrealistic displacement  
21 records. Here we propose a new method using a Kalman filter to estimate coseismic  
22 displacement waveforms using the collocated ocean-bottom seismometers and pressure gauges.  
23 First, we evaluate our method using synthetic records and then apply it to an offshore Mw 6.0  
24 event that generated a small tsunami. In both the synthetic and real cases, our method  
25 successfully estimates reasonable displacement waveforms. Additionally, we show that the  
26 computed waveforms improve the results of the finite fault modeling process. In other words, the  
27 proposed method will be useful for estimating the details of the rupture mechanism of offshore  
28 earthquakes as a complement to onshore observations.

29 **Plain language summary**

30 Ocean-bottom observations enable us to obtain near-fault displacement records associated with  
31 an offshore earthquake. However, simple integration of ocean-bottom acceleration records leads  
32 to physically unrealistic displacement records. Here we propose a new method to estimate  
33 offshore coseismic displacement waveforms. First, we evaluate our method using synthetic  
34 records and then apply it to an offshore earthquake that generated a small tsunami. In both cases,  
35 our method successfully estimates reasonable displacements. Additionally, we show that the  
36 computed waveforms improve the results of the earthquake source modeling process. In other  
37 words, the proposed method will be useful for estimating the details of the rupture mechanism of  
38 offshore earthquakes as a complement to onshore observations.

39

## 40 **1 Introduction**

41 Recently, real-time ocean-bottom seismometer networks have been deployed at active tectonic  
42 margins for the dual purpose of both basic research and real-time monitoring (e.g., S-net and  
43 DONET in Japan, NEPTUNE in Canada, and OOI in the US; Aoi et al., 2020; Barnes & Team,  
44 2007; Trowbridge et al., 2019). These networks enable us to obtain near-fault records associated  
45 with an offshore earthquake. When coseismic deformation is large enough, tsunamis occur due  
46 to such events and can damage coastal areas. Coseismic displacement records at near-fault  
47 stations are thus important because they have the potential to help in evaluating the earthquake  
48 source and its resulting tsunami quickly – this can improve the performance of early warning  
49 systems. In addition, they can be useful in estimating the details of the rupture mechanism of  
50 offshore earthquakes as a complement to onshore observations.

51 The ocean-bottom record has complicated noise sources for seismic recordings of any  
52 kind (e.g., Hilmo & Wilcock, 2020; Webb, 1998), more so than in the onshore environment.  
53 Ideally, we seek to obtain a displacement waveform through the double integrations of an  
54 acceleration or “strong motion” record. However, even in the simpler situation of onshore  
55 recordings, simple integration leads to unphysical results due to “baseline offsets” which are  
56 small shifts in the records (Iwan et al., 1985). Many schemes have been proposed to remove the  
57 drifts in onshore strong-motion records (e.g., Boore, 2001; Wu & Wu, 2007; Wang et al., 2011).  
58 These can often succeed in baseline correction, but their convergence is not always guaranteed,  
59 and even more worrying, even if they do converge it is not always the case that they converge to  
60 the right final static offset (Boore et al., 2002). Additionally, baseline correction is difficult to  
61 apply in real-time settings. Alternatively, Bock et al. (2011) applied a Kalman filter approach to

62 the records of the collocated high-rate Global Navigation Satellite System (HR-GNSS) and  
63 seismometer sites, and succeeded in estimating the displacement waveform. Lately, many papers  
64 expanded on the use of the Kalman filter approach with onshore records (e.g., Geng et al., 2013;  
65 Melgar et al., 2013; Niu & Xu, 2014; Tu et al., 2014; Zang et al., 2019).

66 In this study, we propose a new method to estimate the coseismic displacement  
67 waveforms from offshore strong-motion records. We base the approach on the general  
68 philosophy of Bock et al. (2011): using the Kalman filter and combining the strong-motion  
69 record with the collocated ocean-bottom pressure gauge (OBPG) records. However, we have  
70 added challenges in the offshore environment, since a coseismic OBPG record contains not only  
71 seafloor displacements but also seafloor accelerations, ocean acoustic waves, and tsunamis  
72 (Saito, 2013), we cannot use the same Kalman filter formulation employed for onshore records.  
73 Section 2 explains the innovation of the Kalman filter approach proposed in this study. Then we  
74 apply it to synthetic data (Section 3) and real data for an  $M_w$  6.0 earthquake recorded offshore in  
75 the Nankai, Japan region (Section 4). Finally, in Section 5, the estimated displacement  
76 waveforms are evaluated through the finite fault modeling.

77 Note that our method focuses only on vertical displacement because OBPGs are only  
78 sensitive to physical phenomena that can be leveraged to calculate vertical displacement. Unless  
79 otherwise described all the variables in the later sections are the vertical component.

## 80 **2 Kalman filter implementation**

81 The Kalman filter is an optimal estimation method based on the state-space representation of a  
82 dynamic system (Kalman, 1960). It consists of the combination of two different models: (1) the  
83 dynamic model which captures the physics of the processes involved and describes the time

84 evolution of the states, and (2) the observation model which establishes the relationship between  
 85 measurements and the states. The models used in this study are expressed as:

$$\frac{d}{dt} \begin{bmatrix} d \\ v \\ \Omega \\ \eta \end{bmatrix} = \begin{bmatrix} 0 & 1 & 0 & 0 \\ 0 & 0 & -1 & 0 \\ 0 & 0 & 0 & 0 \\ 0 & 1 & 0 & 0 \end{bmatrix} \begin{bmatrix} d \\ v \\ \Omega \\ \eta \end{bmatrix} + \begin{bmatrix} 0 & 0 \\ 1 & 0 \\ 0 & 0 \\ 0 & 1 \end{bmatrix} \begin{bmatrix} a \\ \dot{h} \end{bmatrix} + \begin{bmatrix} 0 \\ \varepsilon^a \\ \varepsilon^\Omega \\ \varepsilon^{\dot{h}} \end{bmatrix}, \#(1)$$

$$\begin{bmatrix} h \\ \tilde{\eta} \end{bmatrix} = \begin{bmatrix} -1 & 0 & 0 & 1 \\ 0 & 0 & 0 & 1 \end{bmatrix} \begin{bmatrix} d \\ v \\ \Omega \\ \eta \end{bmatrix} + \begin{bmatrix} \varepsilon^h \\ \varepsilon^{\tilde{\eta}} \end{bmatrix}, \#(2)$$

86 where  $d$ ,  $v$ ,  $\eta$ , and  $\Omega$  are the displacement, velocity, tsunami height, and DC offset of  
 87 acceleration. The variables of  $\varepsilon$  are the properties of noise in estimation. The DC offset is  
 88 defined by the difference in baselines between the observed acceleration  $a^{obs}$  and the true  
 89 acceleration  $a^{true}$ :  $\Omega = a^{obs} + \varepsilon^a - a^{true}$  (Melgar et al., 2013). The vector  $[d \ v \ \Omega \ \eta]^T$  is  
 90 thus the state vector, the output or result of the Kalman filter estimator. In this study, we use the  
 91 water-depth fluctuation  $h = \eta - d$  and estimated tsunami height  $\tilde{\eta}$  as the observation (Eq. 2).  
 92 Note that  $\dot{h}$  in Eq. 1 is the time derivative of  $h$ ;  $h$  and  $\tilde{\eta}$  are independently estimated by any  
 93 methods other than the Kalman filter as we'll discuss soon. The noise properties of each variable,  
 94  $\varepsilon$ , are considered to be the Gaussian with zero mean and a standard deviation, i.e.,  $\varepsilon \sim N(0, \sigma)$ ,  
 95 and independent of each other.

96 Because Eqs. 1 and 2 are for continuous time series, an extra step in the derivation is  
 97 needed to discretize them (Lewis et al., 2008):

$$\begin{bmatrix} d_{t+1} \\ v_{t+1} \\ \Omega_{t+1} \\ \eta_{t+1} \end{bmatrix} = \begin{bmatrix} 1 & \Delta t & -\frac{\Delta t^2}{2} & 0 \\ 0 & 1 & -\Delta t & 0 \\ 0 & 0 & 1 & 0 \\ 0 & \Delta t & -\frac{\Delta t^2}{2} & 1 \end{bmatrix} \begin{bmatrix} d_t \\ v_t \\ \Omega_t \\ \eta_t \end{bmatrix} + \begin{bmatrix} \frac{\Delta t^2}{2} & 0 \\ \Delta t & 0 \\ 0 & 0 \\ \frac{\Delta t^2}{2} & \Delta t \end{bmatrix} \begin{bmatrix} a_t \\ \dot{h}_t \end{bmatrix} + q_t, \#(3)$$

$$\begin{bmatrix} h_t \\ \tilde{\eta}_t \end{bmatrix} = \begin{bmatrix} -1 & 0 & 0 & 1 \\ 0 & 0 & 0 & 1 \end{bmatrix} \begin{bmatrix} d_t \\ v_t \\ \Omega_t \\ \eta_t \end{bmatrix} + r_t, \#(4)$$

98 where  $\Delta t$  is the time interval of the dynamic model (0.01 sec in our case, which is the sample  
 99 rate of the ocean bottom accelerometer);  $q_t$  and  $r_t$  are the Gaussian noise such as  $q_t \sim N(0, \mathbf{Q}_t)$   
 100 and  $r_t \sim N(0, \mathbf{R}_t)$ , respectively. The covariance matrices,  $\mathbf{Q}_t$  and  $\mathbf{R}_t$ , are written as:

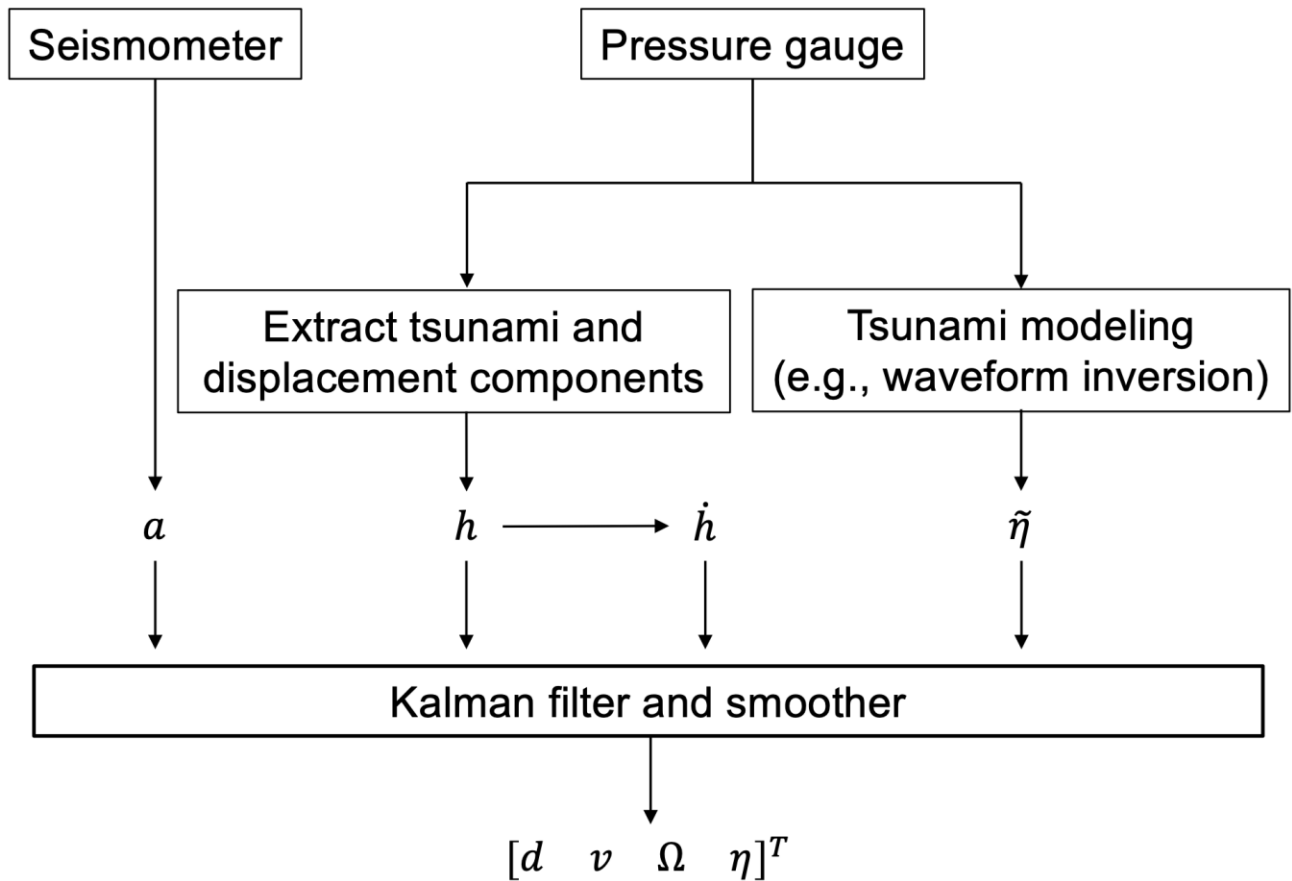
$$\mathbf{Q}_t = \begin{bmatrix} 0 & \sigma_t^a \Delta t^2 / 2 & 0 & 0 \\ \sigma_t^a \Delta t^2 / 2 & \sigma_t^a \Delta t & -\sigma_t^\Omega \Delta t^2 / 2 & \sigma_t^a \Delta t^2 / 2 \\ 0 & -\sigma_t^\Omega \Delta t^2 / 2 & \sigma_t^\Omega \Delta t & 0 \\ 0 & \sigma_t^a \Delta t^2 / 2 & 0 & \sigma_t^h \Delta t \end{bmatrix}, \#(5)$$

$$\mathbf{R}_t = \begin{bmatrix} \sigma_t^h / \Delta \tau & 0 \\ 0 & \sigma_t^{\tilde{\eta}} / \Delta \tau \end{bmatrix}, \#(6)$$

101 where  $\Delta \tau$  is the time interval of the observation model (1 sec in our case, which is the sample  
 102 rate of  $h$  and  $\tilde{\eta}$ ). If  $\Delta t$  and  $\Delta \tau$  are equal, Eqs. 3 and 4 are applied at every time step. If not, Eq. 4  
 103 is only applied when a measurement,  $[h_t \quad \tilde{\eta}_t]^T$ , is available or every  $\Delta \tau$ . Note that as in Bock et  
 104 al. (2011), we apply not only the Kalman filter but also the Kalman smoother which is applied  
 105 backwards in time.

106 Before applying the Kalman filter, we need to obtain  $h$  and  $\tilde{\eta}$  independently of the  
 107 ongoing estimation. In this study, they are estimated by the method proposed by Mizutani et al.  
 108 (2020), extracting the tsunami and displacement components from the coseismic OBPG records

109 on a real-time basis, and the tsunami source model estimated by the tsunami waveform inversion  
 110 using time-derivative waveform (Kubota et al., 2018), respectively (Fig. 1). When calculating  $\tilde{\eta}$ ,  
 111 we assume that the tsunami occurs instantaneously, or, put another way that the rise time for the  
 112 deformation of the seafloor and sea surface can be negligible. The tsunami inversion is  
 113 regularized using spatial smoothing. The weight factor, or the strength of regularization, is  
 114 determined based on the trade-off curve between the variance reduction (VR) and the model  
 115 variance. The details of the inversion methods and the trade-off curves are given in Text S1 and  
 116 Fig. S1.



117  
 118

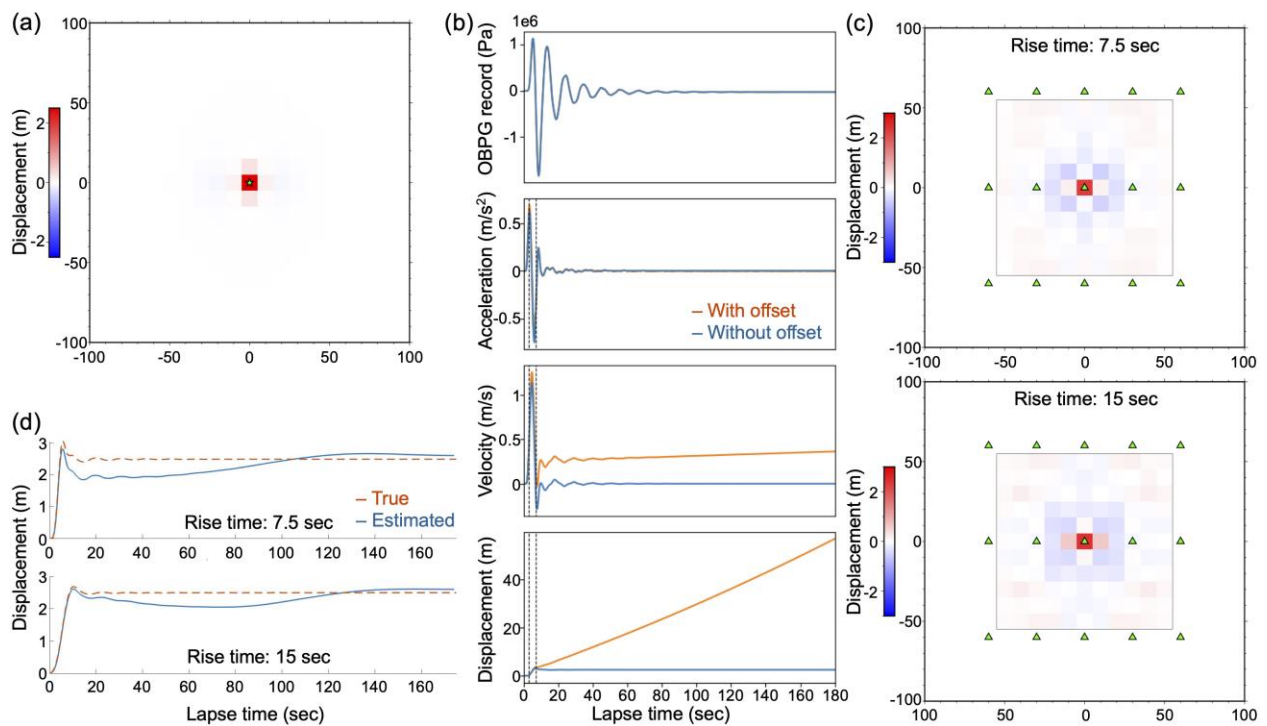
119 **Figure 1.** *The schematic flow of the proposed method.*

120 The covariance matrices,  $\mathbf{Q}_t$  and  $\mathbf{R}_t$ , or the variances of each variable,  $\sigma_t$ , are important  
 121 tuning parameters of the Kalman filter. We propose them to be automatically calculated from the  
 122 records by moving time windows. For the strong-motion records,  $\sigma_t^a$  is the moving variance of  $a$   
 123 and  $\sigma_t^\Omega$  is the absolute value of the moving average of  $a$ ; the 5-sec window is used in both cases.  
 124 Since  $h_t$  is estimated as the difference between two filtered records with a moving taper window  
 125 (Mizutani et al., 2020, Section 5.1),  $\sigma_t^h$  is the sum of the variance of filtered records with the  
 126 range of the taper's flat part (48 sec). Using  $\sigma_t^h$ ,  $\sigma_t^{\tilde{h}}$  is calculated as  $(\sigma_t^h + \sigma_{t-1}^h)/\Delta t$ . Finally,  $\sigma_t^{\tilde{\eta}}$   
 127 is defined as the diagonal elements of  $\mathbf{G}_{\text{forward}}\mathbf{G}_{\text{inv}}^{-1}[\text{cov } \mathbf{p}][\mathbf{G}_{\text{forward}}\mathbf{G}_{\text{inv}}^{-1}]^T$ , where  $\mathbf{G}_{\text{inv}}$  and  
 128  $\mathbf{G}_{\text{forward}}$  are the kernel matrices used in the waveform inversion and forward calculation;  $[\text{cov } \mathbf{p}]$   
 129 is the covariance matrix of the data used in the inversion, that is, the diagonal matrix whose  
 130 elements are  $(\sigma_t^p + \sigma_{t-1}^p)/\Delta\tau$ , where  $\sigma_t^p$  is the moving variance of the data with a time window  
 131 of 60 sec. Note that we do not use  $\sigma_t^p$  but  $(\sigma_t^p + \sigma_{t-1}^p)/\Delta\tau$  because the waveform inversion of  
 132 Kubota et al. (2018) uses time-derivative waveforms.

### 133 **3 Synthetic test**

134 In this section, we confirm the validity of our method and assumptions with synthetic records.  
 135 Based on the methodology of Saito & Tsushima (2016), the records were obtained using  
 136 opensource software for simulating seismic wave propagation, OpenSWPC (Maeda et al., 2017),  
 137 and tsunami propagation, GeoClaw (Clawpack Development Team, 2022; Mandli et al., 2016).  
 138 First, the seafloor acceleration, velocity, displacement, and stress change were calculated by  
 139 OpenSWPC, and then, GeoClaw calculated the tsunami caused by the seafloor movement under  
 140 the non-linear long-wave approximation.

141 A two-layer velocity model was used for the synthetic test: a water layer with P wave  
 142 speed of 1.5 km and density of  $1.0 \text{ kg/m}^3$ ; a homogeneous sea-bottom layer with P and S wave  
 143 speed of 7 and 4 km/s and density of  $2.7 \text{ kg/m}^3$ . The thickness of each layer was 4 and 400 km,  
 144 and the horizontal dimensions of the model domain were  $200 \times 200 \text{ km}$ . The domain was  
 145 divided into 0.5 and 1 km cells in the horizontal and vertical direction, respectively, and the time  
 146 interval was 0.02 sec. The source was represented as a point source whose parameters were as  
 147 follows: the moment magnitude was 7.0; the strike, dip, and rake were  $0^\circ$ ,  $45^\circ$ , and  $90^\circ$  (a pure  
 148 reverse fault); the depth was 10 km; and the rise time was 7.5 sec. We set this source at the  
 149 center of the model domain (Fig. 2a).



150

151 **Figure 2.** (a) Sea-bottom residual displacement in the synthetic test. The Green star represents  
 152 the source location. (b) Synthetic records of ocean-bottom pressure, acceleration, velocity, and  
 153 displacement at the station directly above the source. The blue lines are the records without  
 154 noise. The orange line in the acceleration is with the baseline shift, and the lines in the

155 *displacement and velocity are integrated from it. The black dashed line represents the strong*  
156 *motion duration causing the baseline shift. (c) The result of tsunami waveform inversion for  $\tilde{\eta}$*   
157 *with the rise time of 7.5 sec (top) and 15 sec (bottom). The green triangles and black rectangle*  
158 *represent the stations and target region. (d) Estimated result of the Kalman filter (blue) and true*  
159 *waveform (orange) with the rise time of 7.5 sec (top) and 15 sec (bottom).*

160 Fig. 2b shows the synthetic records directly above the source. The OBPG record had a  
161 large amplitude due to the ocean acoustic waves and sea-bottom acceleration. In acceleration  
162 records, we added the baseline offset based on the model of Iwan et al. (1985), i.e., strong  
163 ground motion causes an offset, and after that, a minor offset still remains. We defined the strong  
164 motion for the baseline shift as over  $0.5 \text{ m/s}^2$ , following Iwan et al. (1985). The offsets during  
165 and after the strong motion were  $0.07$  and  $0.0007 \text{ m/s}^2$ , which were visually adjusted. Although  
166 the baseline shifts slightly affected the acceleration record, they significantly altered the velocity  
167 and displacement records. Note that we applied the Kalman filter to the record at this station;  
168 others were used only for the tsunami inversion.

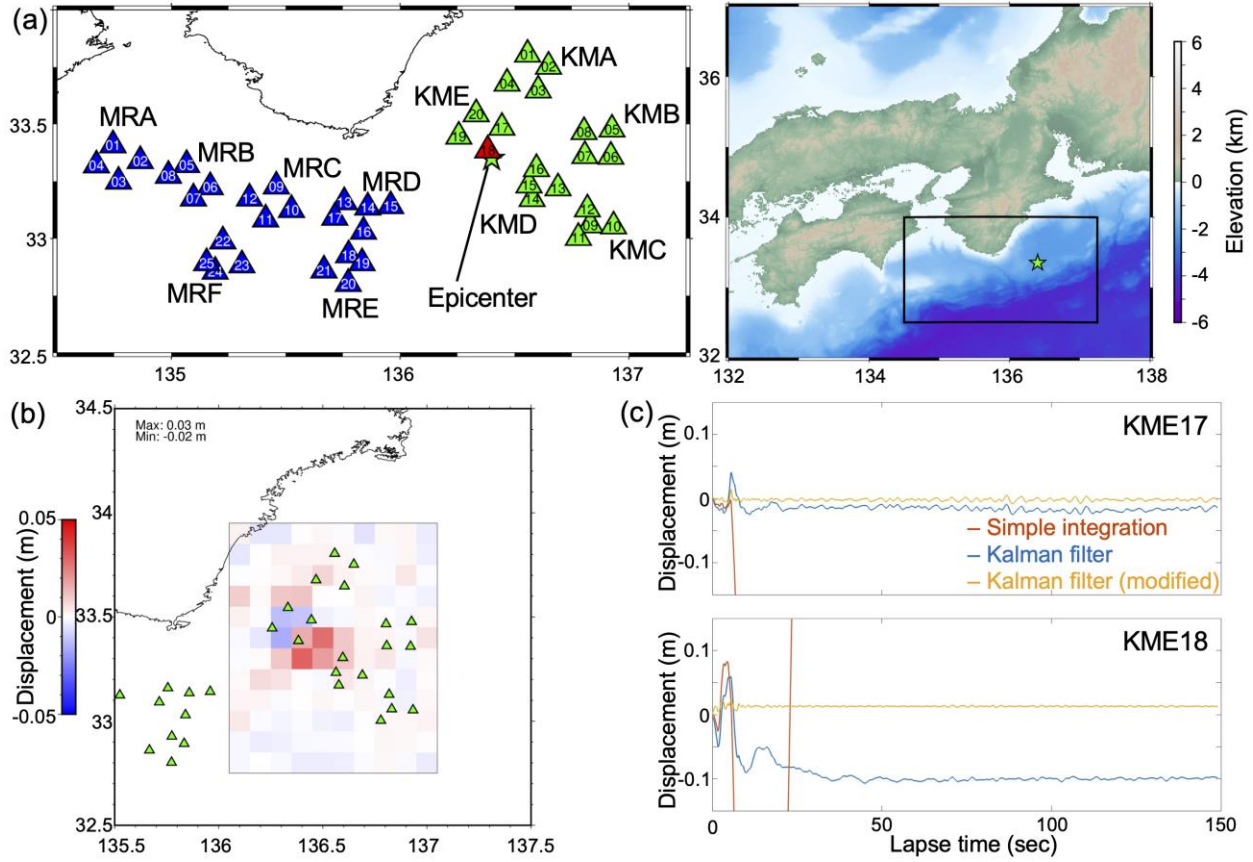
169 The estimated tsunami source model for  $\tilde{\eta}$  and the outcoming results of the Kalman filter  
170 are shown in Figs. 2c and 2d, respectively. Although the input acceleration was contaminated by  
171 the noise, the displacement waveform estimated by our method agreed with the “true” one.

172 When calculating  $\tilde{\eta}$ , our method assumes that a tsunami occurs instantaneously. To  
173 investigate the effect of the rise time, we conducted the same synthetic test with twice the rise  
174 time (15 sec). In this case, the threshold for the baseline shifts in the acceleration was defined as  
175  $0.1 \text{ m/s}^2$ . The resultant waveforms also agreed with the true one, particularly in the dynamic part  
176 of the displacement waveform (Fig. 2d). Since the seafloor and sea surface move simultaneously,  
177 it is difficult for the OBPG to observe any dynamic displacement components, that is, this

178 agreement comes from the acceleration record. In other words, the method proposed in this study  
179 successfully combined the information of the collocated OBPG and strong-motion seismometer.

#### 180 **4 Application to real data**

181 We used the records of Dense Oceanfloor Network system for Earthquakes and Tsunamis  
182 (DONET; Aoi et al., 2020), which is deployed off the coast of Kii Peninsula, Japan (Fig 3a).  
183 Each station of this network consists of an ocean-bottom seismometer and an OBPG. On 1 April  
184 2016, an Mw 6.0 event occurred inside this network (e.g., Araki et al., 2017; Takemura et al.,  
185 2018). The OBPGs clearly observed the pressure change originated from the tsunami, and  
186 strong-motion accelerometer records observed significant shaking (the peak ground acceleration  
187 (PGA) was over  $0.5 \text{ m/s}^2$  at near-fault stations) and contained clear baseline shifts (Kubota et al.,  
188 2018; Mizutani et al., 2020; Wallace et al., 2016). For the preprocessing of the acceleration data,  
189 we removed the pre-earthquake offset in the records by taking the mean of the record 10 sec  
190 before the earthquake. For the OBPG data, the ocean tide component and the offset were  
191 removed by the theoretical tide model (Matsumoto et al., 2000) and the mean of the 30 min of  
192 the pre-event record.



193

194 **Figure 3.** (a) *DONET* stations used in this study. The blue, red, and green triangles are the  
 195 stations used only for the tsunami source inversion, only for the Kalman filter, and for both,  
 196 respectively. Sets of three characters represent the subarrays of *DONET*. The green star is the  
 197 epicenter estimated by Wallace *et al.* (2016). The black rectangle in the right panel represents  
 198 the area of the left panel. (b) Tsunami source model for  $\tilde{\eta}$  estimated by the tsunami waveform  
 199 inversion. (c) Displacement waveforms at stations *KME17* and *KME18* estimated with  $h$  of  
 200 Mizutani *et al.* (2020) (blue) and with  $h$  by the tsunami source inversion (yellow). The Orange  
 201 lines are the displacements simply integrated from the acceleration record.

202

203

204

When conducting the tsunami source inversion for  $\tilde{\eta}$ , we calculated Green's functions  
 with the GEBCO\_2023 bathymetry (GEBCO, 2023) with grid intervals of  $0.02^\circ$  from unit  
 sources which were set each  $0.1^\circ$ . Note that we excluded station *KME18*, the closest station to

205 the source, from the tsunami source inversion as well as Kubota et al. (2018), although applied  
206 the Kalman filter to its record. The resultant model is shown in Fig. 3b.

207 Fig.3c shows the displacement waveforms at stations KME18 and KME17, the second  
208 closest station to the source (the results of other stations are shown in Fig. S2). As with the  
209 synthetic test (Section 3), we succeeded in obtaining stable displacement waveforms. We,  
210 however, must pay attention to the residual displacement or DC component of the waveforms.  
211 For example, the waveform at KME18 indicated a subsidence of about 10 cm. The same signal  
212 was observed in the OBPG record, which previous studies considered as a false signal (Kubota et  
213 al., 2018; Wallace et al., 2016). Since our method estimates the displacement via  $h$  from OBPG  
214 records (Eq. 4), the residual displacement was affected by such an unphysical offset in OBPG  
215 records.

216 To avoid this problem, we changed a method to estimate  $h$  in Eq. 4. We now estimate  $h$   
217 from the same model for  $\tilde{\eta}$ , and the variance  $\sigma_t^h$  was also calculated in the same scheme as  $\tilde{\eta}$ .  
218 Note that this alternative method was applied only to the stations whose OBPG records might  
219 have been contaminated by unphysical offsets: KMA03, KME17, and KME18, as suggested by  
220 Kubota et al. (2018). The displacement waveforms obtained from this method were also stable  
221 (yellow lines in Fig 3c) and the unphysical offsets could be removed. The residual displacements  
222 agreed with the one by the tsunami source inversion.

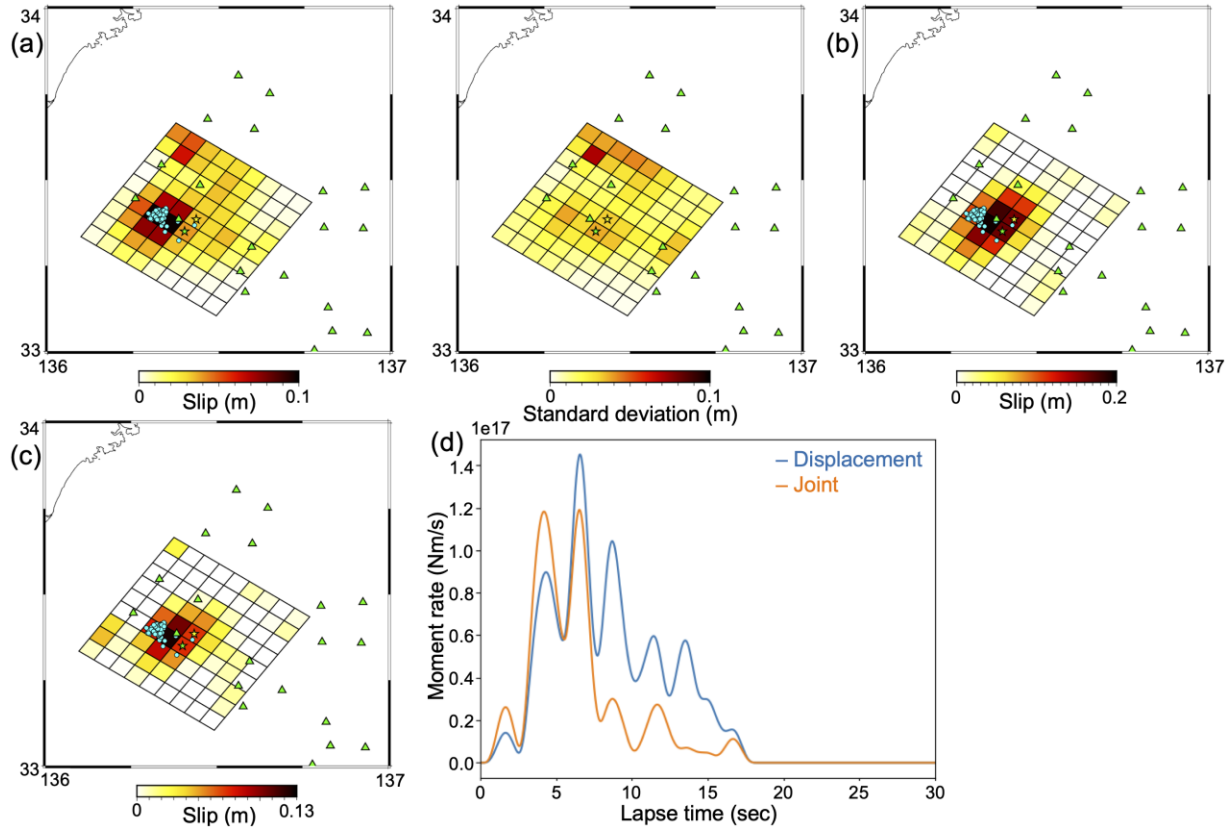
## 223 **5 Finite fault estimation**

224 To evaluate the utility of the displacement waveforms from Section 4, we next conducted a finite  
225 fault inversion and compared the resultant model with the one obtained from the inversion of  
226 tsunami records. We solved this linear inverse problem by the non-negative least square method

227 (Lawson & Hanson, 1995) with spatial smoothing (Text S1 and Fig. S1). Green's functions were  
228 calculated by OpenSWPC and GeoClaw. In the seismic waveform calculation, we used the 3-D  
229 velocity structure model by Koketsu et al. (2012) with grid intervals of 0.25 km and a time step  
230 of 0.01 sec. In the tsunami case, we used the same model in Section 4, i.e., GEBCO\_2023  
231 bathymetry with 0.02° interval.

232 The number of subfaults used was 81, each with a subfault size of  $5 \times 5$  km and a rise  
233 time of 3 sec. Here, we estimated only the slip amount at each subfault; the other fault  
234 parameters were fixed as the values of Wallace et al. (2016): the strike, dip, and rake were 215°,  
235 5°, and 95°; the center of the fault model was at 33.385°N and 136.434°E, and at 9.8 km below  
236 the seafloor. We set the rupture speed to 2.1 km/s, 80 % of the S wave speed in this region  
237 (Kamei et al., 2012; Wallace et al., 2016).

238 Fig. 4a shows the result of the inversion using the displacement waveforms. To  
239 investigate estimation errors, we conducted a bootstrap method with 200 samples where we  
240 randomly selected stations at each iteration (Chernick, 2007). The  $M_w$  calculated from this model  
241 was 5.9 and the VR was 68.7%. From the standard deviation of the bootstrap (right panel in Fig.  
242 4a), a large slip patch beside the epicenter reflects the actual fault slip, while small one close to  
243 station KME20 is perhaps an estimation error. This result is consistent with the aftershock  
244 distribution detected by Japan Meteorological Agency (JMA) and the result from the tsunami-  
245 only inversion (the  $M_w$  and VR were 5.9 and 59%; Fig. 4b). We therefore conclude that the  
246 displacement waveforms estimated in Section 4 can be used reliably for studying offshore  
247 sources.



248

249 **Figure 4.** (a) Slips of the finite fault model (left) and their standard deviations (right) by the  
 250 bootstrap method with displacement waveforms. The green triangles and blue circles represent  
 251 DONET stations and aftershocks larger than magnitude 1 detected by JMA, which occurred  
 252 within two days after the main shock. The green and yellow stars are the epicenter and the fault  
 253 location estimated by Wallace *et al.* (2016). (b)(c) Same as (a) except that by the tsunami  
 254 waveform inversion and by the joint inversion with the displacement and tsunami waveforms. (d)  
 255 The blue and orange lines represent the source time functions calculated by the models of (a)  
 256 and (c).

## 257 6 Discussion

258 To combine displacement and tsunami data, we conducted an additional joint inversion (Text S1  
 259 and Fig. S1). The obtained fault model is shown in Fig. 4c. The VR were 57.1% and 44.1% for

260 the displacement and tsunami; the estimated moment magnitude was 5.8. The model indicated  
261 that the slip propagated from the epicenter to the downdip direction. Compared to the model  
262 from the displacement waveforms only, the fault slip concentrated only around the epicenter. Its  
263 extent was also narrower than the model only using the tsunami.

264 Using the seismic records enables us to calculate the source time function (Fig. 4d). It  
265 indicated that a large rupture occurred at 3 sec after the origin time, and lasted 5 sec. The shorter  
266 duration compared to the one by the model using the displacement only reflects the slip  
267 distribution smaller than that.

268 Wallace et al. (2016) suggested that the aftershocks associated with this event occurred  
269 due to the afterslip immediately following the main shock because their fault model was  
270 separated from the aftershock cluster. Our model, on the other hand, agrees with the aftershock  
271 distribution and indicates that the aftershocks were caused directly by the main shock, that is, the  
272 afterslip may not be necessary for the aftershocks.

273 The aftershock distribution in Fig. 4 concentrates on the west of the slip. This is because  
274 JMA detected the earthquake location using only onshore stations. Araki et al. (2017) found  
275 slow-slip events after this earthquake located in the area between stations KME17 and KME18,  
276 different from the afterslip proposed by Wallace et al. (2016), which cover the north region of  
277 our fault model (Araki et al., 2017, Fig. 2b). In other words, our fault model can explain the  
278 aftershock distribution associated with this event sequence very well.

## 279 **7 Conclusion**

280 We proposed a new method to estimate the coseismic displacement waveform from collocated  
281 ocean-bottom strong-motion accelerometers and OBPGs. Through the synthetic test and the

282 application to real data, we confirmed the displacement waveforms estimated by this method to  
283 be reliable.

284 On the other hand, at some stations close to the epicenter, the resultant waveform had a  
285 relatively large offset due to unphysical DC components in OBPG records. At present, we cannot  
286 remove such an offset automatically because it is difficult to model this offset, that is, cannot be  
287 included simply in the Kalman filter estimation. Although several studies investigated unphysical  
288 drifts in OBPG records, they focused on the static records (Chadwick et al., 2006; Hino et al.,  
289 2022). Clarifying the characteristics of coseismic OBPG records will improve the Kalman filter  
290 approach to ocean-bottom records.

291 The finite fault model that jointly inverted from both the displacement and tsunami  
292 waveforms showed improvements compared to the models estimated independently. In other  
293 words, the displacement waveform by our method can help us to reveal the details of the rupture  
294 process of offshore earthquakes.

295

## 296 **Acknowledgments**

297 The records of DONET used in this study were provided by the NIED. This work benefitted  
298 from access to the University of Oregon high performance computing cluster, Talapas. This  
299 work was partially supported by JSPS KAKENHI grant number 22J10212.

300

## 301 **Open Research**

302 DONET records (NIED, 2019) can be downloaded from the NIED website  
303 (<https://www.hinet.bosai.go.jp/?LANG=en>, for strong-motion records;  
304 <https://www.seafloor.bosai.go.jp>, for pressure records) with data request and permission. The  
305 codes of OpenSWPC and GeoClaw are freely available from GitHub  
306 (<https://tktmyd.github.io/OpenSWPC/> and <https://github.com/clawpack>).

307

## 308 **References**

- 309 Aoi, S., Asano, Y., Kunugi, T., Kimura, T., Uehira, K., Takahashi, N., Ueda, H., Shiomi, K.,  
310 Matsumoto, T., & Fujiwara, H. (2020). MOWLAS: NIED observation network for earthquake,  
311 tsunami and volcano. *Earth, Planets and Space*, 72(1), 126. [https://doi.org/10.1186/s40623-020-](https://doi.org/10.1186/s40623-020-01250-x)  
312 01250-x
- 313 Araki, E., Saffer, D. M., Kopf, A. J., Wallace, L. M., Kimura, T., Machida, Y., Ide, S., Davis, E.,  
314 & IODP EXPEDITION 365 SHIPBOARD SCIENTISTS. (2017). Recurring and triggered slow-  
315 slip events near the trench at the Nankai Trough subduction megathrust. *Science*, 356(6343),  
316 1157–1160. <https://doi.org/10.1126/science.aan3120>
- 317 Barnes, C. R., & Team, N. C. (2007). Building the World’s First Regional Cabled Ocean  
318 Observatory (NEPTUNE): Realities, Challenges and Opportunities. *OCEANS 2007*, 1–8.  
319 <https://doi.org/10.1109/OCEANS.2007.4449319>
- 320 Bock, Y., Melgar, D., & Crowell, B. W. (2011). Real-Time Strong-Motion Broadband  
321 Displacements from Collocated GPS and Accelerometers. *Bulletin of the Seismological Society*  
322 *of America*, 101(6), 2904–2925. <https://doi.org/10.1785/0120110007>

- 323 Boore, D. M. (2001). Effect of baseline corrections on displacements and response spectra for  
324 several recordings of the 1999 Chi-Chi, Taiwan, earthquake. *Bulletin of the Seismological*  
325 *Society of America*, 91(5), 1199–1211.
- 326 Boore, D. M., Stephens, C. D., & Joyner, W. B. (2002). Comments on Baseline Correction of  
327 Digital Strong-Motion Data: Examples from the 1999 Hector Mine, California, Earthquake.  
328 *Bulletin of the Seismological Society of America*, 92(4), 1543–1560.  
329 <https://doi.org/10.1785/0120000926>
- 330 Chadwick, W., Nooner, S., Zumberge, M., Embley, R., & Fox, C. (2006). Vertical deformation  
331 monitoring at Axial Seamount since its 1998 eruption using deep-sea pressure sensors. *Journal*  
332 *of Volcanology and Geothermal Research*, 150, 313–327.
- 333 Chernick, M. (2007). *Bootstrap Methods: A Guide for Practitioners and Researchers*. Wiley.
- 334 Clawpack Development Team. (2022). *Clawpack software*.  
335 <https://doi.org/10.5281/zenodo.7026045>
- 336 GEBCO. (2023). *The General Bathymetric Chart of the Oceans* [dataset].  
337 <https://doi.org/10.5285/f98b053b-0cbc-6c23-e053-6c86abc0af7b>
- 338 Geng, J., Bock, Y., Melgar, D., Crowell, B. W., & Haase, J. S. (2013). A new seismogeodetic  
339 approach applied to GPS and accelerometer observations of the 2012 Brawley seismic swarm:  
340 Implications for earthquake early warning. *Geochemistry, Geophysics, Geosystems*, 14(7), 2124–  
341 2142. <https://doi.org/10.1002/ggge.20144>

- 342 Hilmo, R., & Wilcock, W. S. D. (2020). Physical Sources of High-Frequency Seismic Noise on  
343 Cascadia Initiative Ocean Bottom Seismometers. *Geochemistry, Geophysics, Geosystems*,  
344 *21*(10), e2020GC009085. <https://doi.org/10.1029/2020GC009085>
- 345 Hino, R., Kubota, T., Chikasada, N. Y., Ohta, Y., & Otsuka, H. (2022). Assessment of S-net  
346 seafloor pressure data quality in view of seafloor geodesy. *Progress in Earth and Planetary*  
347 *Science*, *9*(1), 73. <https://doi.org/10.1186/s40645-022-00526-y>
- 348 Iwan, W. D., Moser, M. A., & Peng, C.-Y. (1985). Some observations on strong-motion  
349 earthquake measurement using a digital accelerograph. *Bulletin of the Seismological Society of*  
350 *America*, *75*(5), 1225–1246.
- 351 Kalman, R. E. (1960). A New Approach to Linear Filtering and Prediction Problems. *Journal of*  
352 *Basic Engineering*, *82*(1), 35–45. <https://doi.org/10.1115/1.3662552>
- 353 Kamei, R., Pratt, R. G., & Tsuji, T. (2012). Waveform tomography imaging of a megasplay fault  
354 system in the seismogenic Nankai subduction zone. *Earth and Planetary Science Letters*, *317*–  
355 *318*, 343–353. <https://doi.org/10.1016/j.epsl.2011.10.042>
- 356 Koketsu, K., Miyake, H., & Suzuki, H. (2012). *Japan Integrated Velocity Structure Model*  
357 *Version 1*. The 15th World Conference on Earthquake Engineering, Lisboa.  
358 [https://www.iitk.ac.in/nicee/wcee/article/WCEE2012\\_1773.pdf](https://www.iitk.ac.in/nicee/wcee/article/WCEE2012_1773.pdf)
- 359 Kubota, T., Suzuki, W., Nakamura, T., Chikasada, N. Y., Aoi, S., Takahashi, N., & Hino, R.  
360 (2018). Tsunami source inversion using time-derivative waveform of offshore pressure records  
361 to reduce effects of non-tsunami components. *Geophysical Journal International*, *215*(2), 1200–  
362 1214. <https://doi.org/10.1093/gji/ggy345>

363 Lawson, C., & Hanson, R. (1995). *Solving least squares problems*. Society for Industrial and  
364 Applied Mathematics.

365 Lewis, F., Xie, L., & Popa, D. (2008). *Optimal and Robust Estimation: With an Introduction to*  
366 *Stochastic Control Theory* (2nd ed.). CRC Press.

367 Maeda, T., Takemura, S., & Furumura, T. (2017). OpenSWPC: An open-source integrated  
368 parallel simulation code for modeling seismic wave propagation in 3D heterogeneous  
369 viscoelastic media. *Earth, Planets and Space*, 69(1), 102. [https://doi.org/10.1186/s40623-017-](https://doi.org/10.1186/s40623-017-0687-2)  
370 0687-2

371 Mandli, K. T., Ahmadi, A. J., Berger, M., Calhoun, D., George, D. L., Hadjimichael, Y.,  
372 Ketcheson, D. I., Lemoine, G. I., & LeVeque, R. J. (2016). Clawpack: Building an open source  
373 ecosystem for solving hyperbolic PDEs. *PeerJ Computer Science*, 2, e68.  
374 <https://doi.org/10.7717/peerj-cs.68>

375 Matsumoto, K., Takanezawa, T., & Ooe, M. (2000). Ocean tide models developed by  
376 assimilating TOPEX/POSEIDON altimeter data into hydrodynamical model: A global model and  
377 a regional model around Japan. *Journal of Oceanography*, 56(5), 567–581.

378 Melgar, D., Bock, Y., Sanchez, D., & Crowell, B. W. (2013). On robust and reliable automated  
379 baseline corrections for strong motion seismology. *Journal of Geophysical Research: Solid*  
380 *Earth*, 118(3), 1177–1187. <https://doi.org/10.1002/jgrb.50135>

381 Mizutani, A., Yomogida, K., & Tanioka, Y. (2020). Early Tsunami Detection With Near-Fault  
382 Ocean-Bottom Pressure Gauge Records Based on the Comparison With Seismic Data. *Journal of*  
383 *Geophysical Research: Oceans*, 125(9), e2020JC016275. <https://doi.org/10.1029/2020JC016275>

- 384 National Research Institute for Earth Science and Disaster Resilience (NIED). (2019). *NIED*  
385 *DONET*. <https://doi.org/10.17598/nied.0008>
- 386 Niu, J., & Xu, C. (2014). Real-Time Assessment of the Broadband Coseismic Deformation of the  
387 2011 Tohoku-Oki Earthquake Using an Adaptive Kalman Filter. *Seismological Research Letters*,  
388 85(4), 836–843. <https://doi.org/10.1785/0220130178>
- 389 Saito, T. (2013). Dynamic tsunami generation due to sea-bottom deformation: Analytical  
390 representation based on linear potential theory. *Earth, Planets and Space*, 65(12), 1411–1423.
- 391 Saito, T., & Tsushima, H. (2016). Synthesizing ocean bottom pressure records including seismic  
392 wave and tsunami contributions: Toward realistic tests of monitoring systems. *Journal of*  
393 *Geophysical Research: Solid Earth*, 121(11), 8175–8195. <https://doi.org/10.1002/2016JB013195>
- 394 Takemura, S., Kimura, T., Saito, T., Kubo, H., & Shiomi, K. (2018). Moment tensor inversion of  
395 the 2016 southeast offshore Mie earthquake in the Tonankai region using a three-dimensional  
396 velocity structure model: Effects of the accretionary prism and subducting oceanic plate. *Earth,*  
397 *Planets and Space*, 70(1), 50. <https://doi.org/10.1186/s40623-018-0819-3>
- 398 Trowbridge, J., Weller, R., Kelley, D., Dever, E., Plueddemann, A., Barth, J. A., & Kawka, O.  
399 (2019). The Ocean Observatories Initiative. *Frontiers in Marine Science*, 6.  
400 <https://www.frontiersin.org/articles/10.3389/fmars.2019.00074>
- 401 Tu, R., Wang, R., Walter, T. R., & Diao, F. (2014). Adaptive recognition and correction of  
402 baseline shifts from collocated GPS and accelerometer using two phases Kalman filter. *Advances*  
403 *in Space Research*, 54(9), 1924–1932. <https://doi.org/10.1016/j.asr.2014.07.008>

- 404 Wallace, L. M., Araki, E., Saffer, D., Wang, X., Roesner, A., Kopf, A., Nakanishi, A., Power,  
405 W., Kobayashi, R., & Kinoshita, C. (2016). Near-field observations of an offshore Mw 6.0  
406 earthquake from an integrated seafloor and subseafloor monitoring network at the Nankai trough,  
407 southwest Japan. *Journal of Geophysical Research: Solid Earth*, *121*(11), 8338–8351.
- 408 Wang, R., Schurr, B., Milkereit, C., Shao, Z., & Jin, M. (2011). An Improved Automatic Scheme  
409 for Empirical Baseline Correction of Digital Strong-Motion Records. *Bulletin of the*  
410 *Seismological Society of America*, *101*(5), 2029–2044. <https://doi.org/10.1785/0120110039>
- 411 Webb, S. C. (1998). Broadband seismology and noise under the ocean. *Reviews of Geophysics*,  
412 *36*(1), 105–142. <https://doi.org/10.1029/97RG02287>
- 413 Wu, Y.-M., & Wu, C.-F. (2007). Approximate recovery of coseismic deformation from Taiwan  
414 strong-motion records. *Journal of Seismology*, *11*(2), 159–170.
- 415 Zang, J., Xu, C., Chen, G., Wen, Q., & Fan, S. (2019). Real-time coseismic deformations from  
416 adaptively tight integration of high-rate GNSS and strong motion records. *Geophysical Journal*  
417 *International*, *219*(3), 1757–1772. <https://doi.org/10.1093/gji/ggz397>
- 418



*[Geophysical Research Letters]*

Supporting Information for

**Strong-motion Broadband Displacements from Collocated Ocean-bottom Pressure Gauges and Seismometers**

A. Mizutani<sup>1, 2</sup>, D. Melgar<sup>2</sup>, K. Yomogida<sup>1</sup>

<sup>1</sup>Department of Earth and Planetary Sciences, Faculty of Sciences, Hokkaido University, Sapporo, Japan, <sup>2</sup>Department of Earth Sciences, University of Oregon, Eugene, Oregon, U.S.A.

**Contents of this file**

Text S1  
Figures S1 to S2

**Introduction**

Text S1 explains the details of the inversion methods in the main article. Fig. S1 shows the trade-off curves used to determine the weight in the inversion. Fig. S2 shows the displacement waveforms estimated by the proposed method at all the stations.

**Text S1.**

In the main text, we conducted three kinds of inversions: the tsunami source inversion (Section 2), the finite fault inversion (Section 5), and the joint inversion (Section 6). The first two solve the equation below:

$$\begin{bmatrix} \mathbf{d} \\ \mathbf{0} \end{bmatrix} = \begin{bmatrix} \mathbf{G} \\ \alpha \mathbf{S} \end{bmatrix} \mathbf{m}, \quad (\text{S1})$$

where  $\mathbf{d}$ ,  $\mathbf{G}$ ,  $\mathbf{S}$ , and  $\mathbf{m}$  are the data vector, kernel matrix, spatial smoothing matrix, and model vector, respectively. The weight parameter  $\alpha$  is determined based on the trade-off curve of the variance reduction (VR) and model variance. In this study, the variance reduction is defined as (Takemura et al., 2018):

$$VR = \left( 1 - \frac{\sum_i \int [u_i^{OBS}(t) - u_i^{SYN}(t)]^2 dt}{\sum_i \int [u_i^{OBS}(t)]^2 dt} \right) \times 100 [\%], \quad (\text{S2})$$

where  $u_i^{OBS}(t)$  and  $u_i^{SYN}(t)$  are the observed and synthetic waveforms at station  $i$ . The trade-off curves of each result are shown in Fig. S1.

The tsunami source inversion is based on Kubota et al (2018). We first take the moving average with a time window of 60 sec and then apply a low-pass filter of 100 sec to the ocean-bottom pressure records. The time-derivative waveforms of them are used as the data and Green's functions. We set the record length to 25 min. The singular value decomposition is used to solve Eq. S1.

In the finite fault inversion, we solve Eq. 1 by the non-negative least squares method (Lawson & Hanson, 1995). For the tsunami data, we apply the same preprocessing as in the tsunami source inversion. For the displacement data, we apply a low-pass filter of 20 sec and use 30 sec from the origin time.

In the joint inversion, Eq. 1 is modified to:

$$\begin{bmatrix} \mathbf{d}_{DIPS} \\ \mathbf{d}_{TSUN} \\ \mathbf{0} \end{bmatrix} = \begin{bmatrix} \frac{W_{DISP}}{N_{OBS}} \mathbf{G}_{DISP} \\ \frac{W_{TSUN}}{N_{OBPG}} \mathbf{G}_{TSUN} \\ \alpha \mathbf{S} \end{bmatrix} \mathbf{m}, \quad (\text{S3})$$

where  $\mathbf{d}_{DISP}$ ,  $\mathbf{G}_{DISP}$ , and  $W_{DISP}$  are the data vector, kernel matrix, and weight for the displacement records;  $\mathbf{d}_{TSUN}$ ,  $\mathbf{G}_{TSUN}$ , and  $W_{TSUN}$  are the same except that for the tsunami records;  $N_{OBS}$  and  $N_{OBPG}$  are the number of ocean-bottom seismometers and ocean-bottom pressure gauges. The preprocessing for data is the same as the above. The weights are also decided by the trade-off curve.

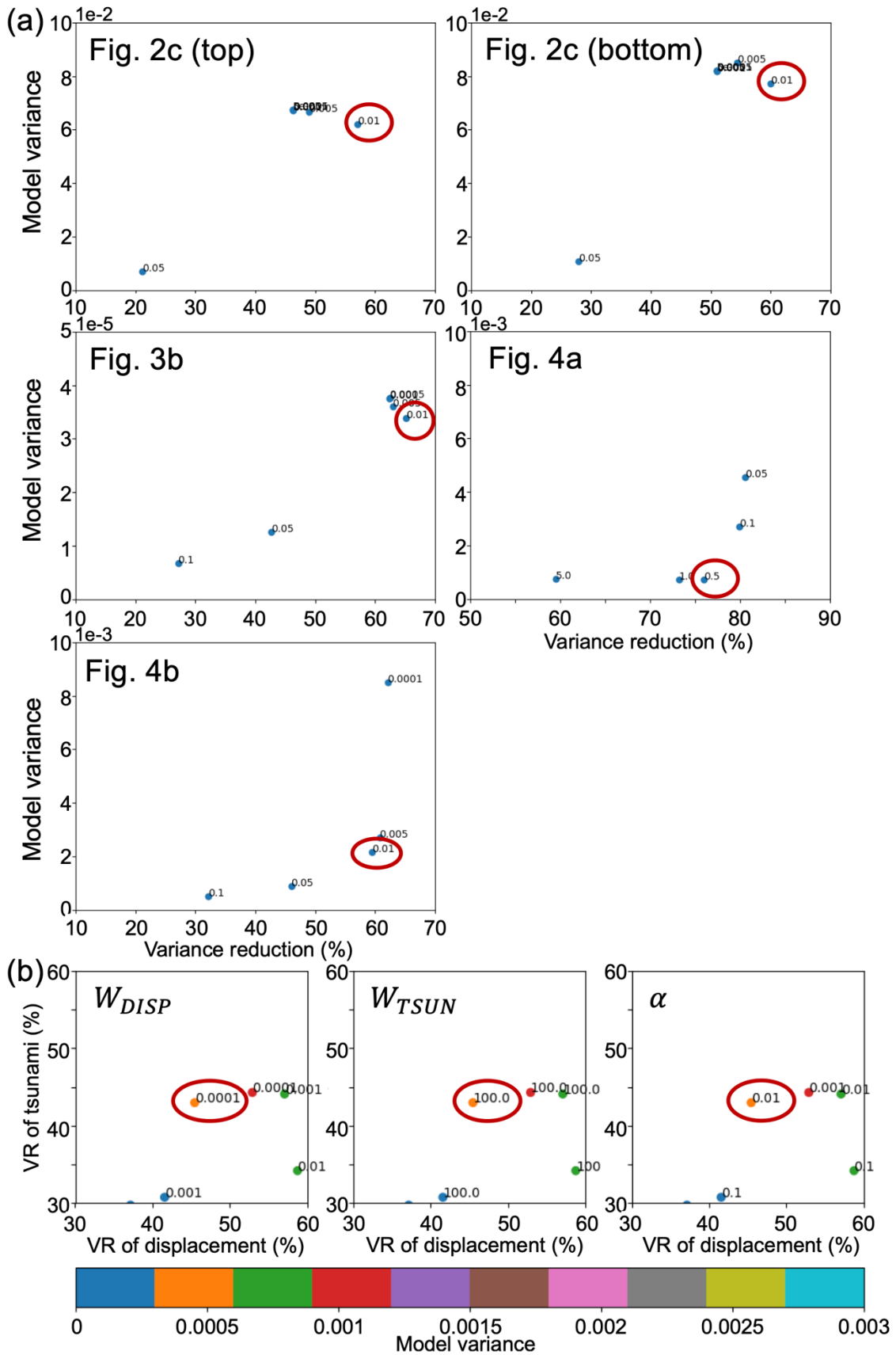


**Figure S1.** (a) Trade-off curves used to determine the weight  $\alpha$  in the inversions of Figs. 2c, 3b, 4a, and 4b. The text at each point is  $\alpha$  in Eq. S1, and the red circles represent the weight we used. Note that although the result of Fig.4a comes from the bootstrap method, the trade-off curve is obtained by the single inversion. That is why the VR value is different from the main text. (b) Trade-off curves for the joint inversion (Fig. 4c). The left, center, and right panels are for  $W_{DIPS}$ ,  $W_{TSUN}$ , and  $\alpha$  in Eq. S3, respectively. The text and color of each point indicates the weight and model variance.

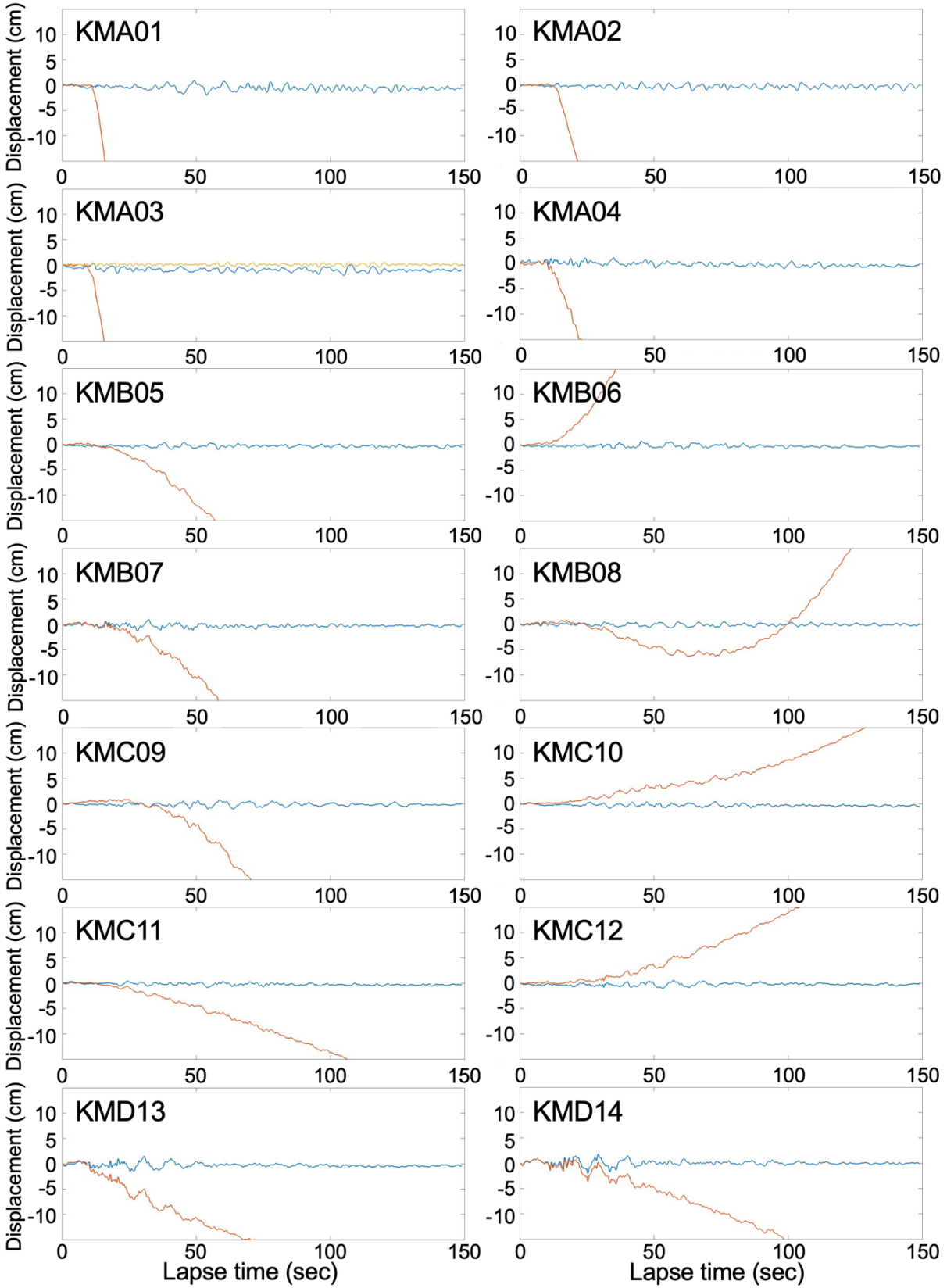


**Figure S2.** Same as Fig. 3c except that at all other stations.

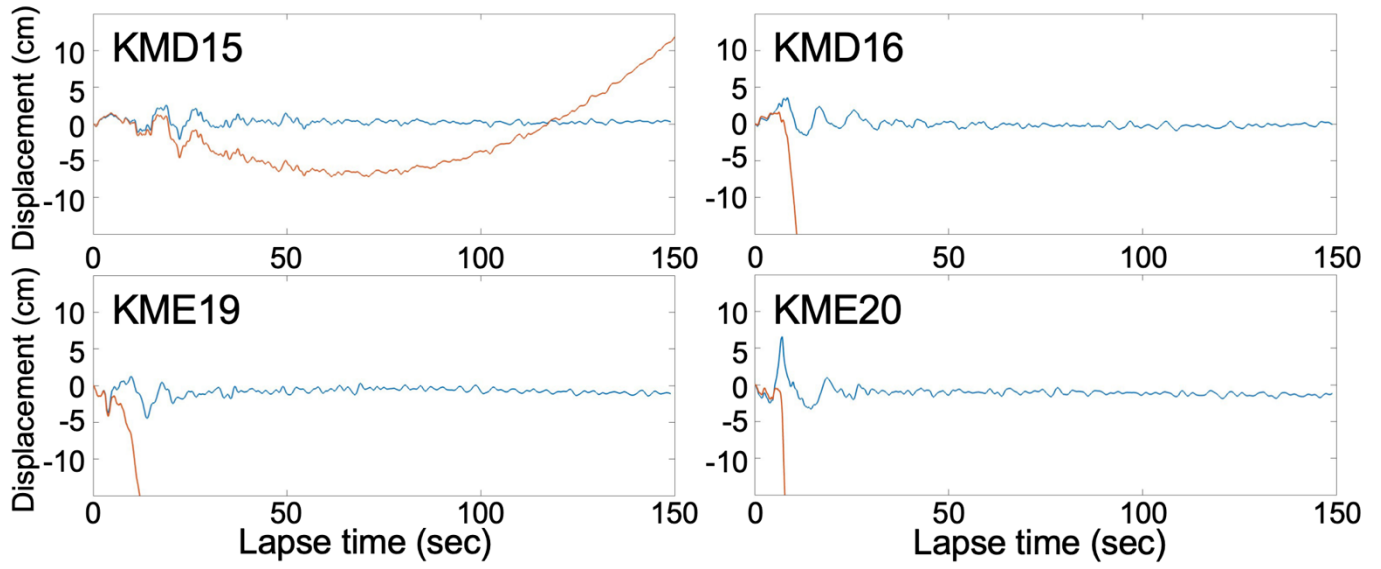


**Figure S2.** (Continued)

## References

Kubota, T., Suzuki, W., Nakamura, T., Chikasada, N. Y., Aoi, S., Takahashi, N., & Hino, R. (2018). Tsunami source inversion using time-derivative waveform of offshore pressure records to reduce effects of non-tsunami components. *Geophysical Journal International*, 215(2), 1200–1214. <https://doi.org/10.1093/gji/ggy345>

Lawson, C., & Hanson, R. (1995). *Solving least squares problems*. Society for Industrial and Applied Mathematics.

Takemura, S., Kimura, T., Saito, T., Kubo, H., & Shiomi, K. (2018). Moment tensor inversion of the 2016 southeast offshore Mie earthquake in the Tonankai region using a three-dimensional velocity structure model: Effects of the accretionary prism and subducting oceanic plate. *Earth, Planets and Space*, 70(1), 50. <https://doi.org/10.1186/s40623-018-0819-3>